8A.5

INVESTIGATION OF A CELL MERGER ACCOMPANYING CYCLIC TORNADO PRODUCTION

Robin L. Tanamachi*[,1,2]
Pamela L. Heinselman[2]
Louis J. Wicker[2]

[1]Cooperative Institute for Mesoscale Meteorological Studies, The University of Oklahoma, Norman, Oklahoma

[2]NOAA / OAR National Severe Storms Laboratory, Norman, Oklahoma

1. INTRODUCTION

Storm mergers frequently occur during tornadic thunderstorm outbreaks. From an operational (dynamical) standpoint, a storm merger occurs when two radar reflectivity objects (updrafts) unite. Anecdotal evidence suggests that storm mergers may affect the occurrence and timing of subsequent tornadoes. While it is often postulated that storm mergers may enhance tornado production potential (Lee et al. 2006), there are also documented instances in which tornado production appears to slow or cease following a merger (e.g., Lindsey and Bunkers 2005), or in which a merger is associated with the disruption of an ongoing tornado (e.g., Wurman et al. 2007). Two hypotheses to explain these observations are summarized in Fig. 1.

A relatively small number of formal observational studies (e.g., references above) have examined the associations between storm mergers and tornado formation, maintenance, and dissipation. There are two primary reasons for this dearth of formal literature. First, it is increasingly evident from the results of tornado research field projects (e.g., VORTEX and VORTEX2) that the processes governing tornadogenesis potentially occur on time scales of a minute or less (e.g., Dowell and Bluestein 2002b; Wakimoto et al. 2011; French et al. 2013), but WSR-88D observations are collected at relatively coarse spatial (~ 1-km range gate spacing) and temporal (4.1-min) scales. In addition, comprehensive higher-spatiotemporal-resolution data sets such as those from mobile Doppler radars (Dowell and Bluestein 2002a; Wurman et al. 2007; Hastings et al. 2010) are relatively rare. Second, a dynamical study of a storm merger requires knowledge of the updrafts, but vertical velocity (w) is poorly observed by most terrestrial radars and must be inferred through some type of analysis.

Cell mergers have been studied using idealized three-dimensional numerical simulations (e.g., Klemp et al. 1980; Kogan and Shapiro 1996; Bluestein and Weisman 2000; Jewett et al. 2002). Hastings and Richardson (2010) attempted to artificially instigate storm mergers by "targeting" pairs of simulated storms for collision. They found that mergers between more mature storms resulted in stronger vertical velocity and vertical vorticity (ς) maxima than mergers between younger storms, in spite of the possible mitigating effects of expanding cold pools. In an expansion of that work, Hastings et al. (2012) sorted simulated mergers between mature and nascent supercells into four categories, one of which ("Type III") frequently exhibited a "bridging" updraft developing between merging updrafts and ended with a classic supercell. This evolution was analogous to one class of the related phenomenon of cloud mergers (Westcott and Kennedy 1989).

In the present study, we investigate the dynamics of a storm merger that occurred during the central Oklahoma tornadic thunderstorm outbreak of 24 May 2011. Specifically, we examine the merger between the tornadic El Reno, Oklahoma storm (a.k.a., "Storm B"; see National Weather Service 2012) and a younger, nontornadic, merging storm, which occurred as one tornado ("B1"; 2031 – 2046 UTC) dissipated and a second, long-tracked tornado ("B2"; 2050 – 2135 UTC) developed (Fig. 2). We seek to develop a coherent portrait of the merger and any resultant changes in the low-level and midlevel mesocyclones (LLMs and MLMs, respectively)

* *Corresponding author's current affiliation*: Robin L. Tanamachi; Cooperative Institute for Mesoscale Meteorological Studies; 120 David L. Boren Blvd.; Norman, OK 73072; e-mail: robin.tanamachi@noaa.gov

in the El Reno storm. We accomplish this by assimilating rapid (~1-min) volumetric observations of the El Reno storm into a numerical cloud model, qualitatively verify them against similarly frequent surface observations (among others), and then objectively identify pertinent dynamical features of the merger process.

2. DATA AND METHODOLOGY

Our primary data set is the reflectivity (*Z*) and Doppler velocity (V_r) observations of the El Reno storm collected by the National Weather Radar Testbed Phased Array Radar (PAR; Zrnić et al. 2007; Heinselman et al. 2008; Heinselman and Torres 2011). The PAR V_r observations were dealiased manually; some ground clutter and other nonmeteorological artifacts were also manually removed (K. Manross, personal communication, 2013) using Solo (Oye et al. 1995). Prior to assimilation, the *Z* and V_r observations were objectively analyzed onto a 4 km grid using a Cressman (1959) objective analysis scheme with a 2.8-km radius of influence. The analyzed radar data remained on the co-plane surface of the radar sweep so that no vertical interpolation or averaging was introduced.

We simulated the storms using the NSSL Collaborative Model for Multiscale Atmospheric Simulation (NCOMMAS; Coniglio et al. 2006), using the Local Ensemble Transform Kalman Filter (LETKF; Ott et al. 2004; Hunt et al. 2007) technique to assimilate the PAR *Z* and V_r observations and constrain the analyses. The domain (Fig. 3a) was specified so that the El Reno storm's hook would be near the center at the time of the merger and handoff (Fig. 3b). The horizontal grid spacing (1 km; Table 1) is insufficient to resolve tornadoes, but is sufficient to resolve mesocyclones (2 – 6 km diameter).

The sounding used to initialize the ensemble was taken from the grid point closest to Binger, Oklahoma from the 40-km Rapid Update Cycle (RUC) 2000 UTC model run at 2100 UTC (e.g., a one-hour forecast, Fig. 3c). This sounding, which featured surface-based CAPE in excess of 4500 J kg^{-1}, 0-to-6 km wind shear magnitude of 27 m s^{-1} (Fig. 3d), was felt to be representative of the inflow profile of the El Reno storm. To initialize the ensemble of horizontally homogeneous storm environments with some uncertainty, a uniform distribution of random perturbations with an amplitude of 2.5 m s^{-1} were added to each ensemble member's *u* and *v* base state winds. To initiate convection, 10 ellipsoidal "perturbation blobs" (within which potential temperature [θ], *u*, *v*, *w*, and water vapor mixing ratio [q_v] were perturbed by small amounts) were placed in the south central portion of the domain in a narrow rectangular region where active convection was already occurring.

Each ensemble member was initialized at 1930 UTC, and allowed to integrate freely for 10 min. Then, Twin Lakes, Oklahoma WSR-88D (KTLX), *Z* and V_r observations were assimilated every 5 min from 1940 to 1955 UTC (i.e., approximately four KTLX volumes), and model integration stopped at 2000 UTC. The early KTLX data assimilation populated the ensemble with heterogeneous, well-spread model states to serve as initial conditions (Stensrud and Gao 2010) for the PAR data assimilation starting at 2000 UTC.

Starting at 2000 UTC, both PAR *Z* and V_r observations were assimilated synchronously every 1 min. We mitigated detrimental effects of frequent *Z* assimilation (Dowell et al. 2011) by assuming a relatively large observation error for *Z* (σ_z = 10 dBZ). Ensemble spread was maintained through the application of additive noise every five minutes while adaptive inflation (Miyoshi 2010) was applied as part of each data assimilation cycle.

With NCOMMAS analyses produced every minute, it was necessary to automate objective identification of features of interest (storms, mesocyclones, updrafts) within the domain. In addition, because of the size and intensity differences among the objects being identified (e.g., mature supercells versus developing storms), we wanted to use an automated technique that could satisfactorily identify objects in a manner similar to a trained human observer. We used the enhanced watershed algorithm (Lakshmanan et al. 2009) on horizontal slices of the ensemble mean analysis, identifying *Z* objects ("storms"), positive *w* objects ("updrafts"), and ς objects ("vortices") using the parameters shown in Table 2. We then used a tracking algorithm ("NEW"; Lakshmanan and Smith 2010) to associate these objects across time. This was done to reduce subjectivity in the identification of occasionally-transient features like the LLM, MLM, and updrafts.

3. QUALITATIVE VERIFICATION

The resulting forecast fields contain two or three powerful supercells in the northern and central portions of the domain (Fig. 3b), including the El Reno storm. The ensemble mean (Fig. 4g – l and s – x) accurately depicts overall storm location and movement as seen by the PAR (Fig. 4a – f and m – r). In particular, the simulated cell merger into the right flank of the El Reno storm (Fig. 4i – l and s – x) is well represented in terms of time and location when compared with that in the PAR *Z* observations (Fig. 2; Fig. 4c – f and m – r).

Owing to the spatial and temporal density of the PAR data set for this case, we were able to assimilate a full volume of radar data every minute, strongly constraining the ensemble analysis. Furthermore, we found good correspondence (given the data spacing) between the locations of analyzed updrafts and enhanced differential reflectivity (Z_{DR}) columns (Illingworth et al. 1987; Kumjian and Ryzhkov 2008; Romine et al. 2008) observed by a dual-polarized WSR-88D that is almost collocated with the PAR (KOUN) (Snyder et al. 2014; this volume). Thus, in this particular case, we have high confidence that the structures and locations of storm features are reasonably represented.

a. Comparison with rotation tracks

We generated a vorticity swath (Dawson et al. 2012) at 1 km AGL to compare with independent indicators of rotation. The swath, which at each grid point is the percentage of ensemble members experiencing time-integrated maximum vorticity exceeding a set threshold (0.02 s^{-1}, in our case), can be interpreted as an indicator of the probability of a strong LLM. We have broken the swath up into five segments (labeled V1 through V5 in Fig. 5a) for ease of discussion. Overall, the locations of the swath and the surface damage track (Fig. 5a) corresponded well, but did exhibit some localized differences. In particular, the swath indicates strong low-level rotation was likely southwest of the start of Tornado B1's damage track (swath V1), where no surface damage was found, as well as directly above the gap between the tracks of Tornadoes B1 and B2 (swath V3). Additionally, the vorticity swaths corresponding to Tornado B2 (swaths V3 through V5) are displaced a few km to the north of the surface damage track. We are not particularly troubled by these displacements, because tornadoes have often been observed to tilt with height (e.g., Wakimoto and Atkins 1996).

As an independent proxy for the LLM track, we used a radar-derived, low-level (0-3 km) rotation track (Miller et al. 2012) generated primarily from KTLX and Vance Air Force Base, Oklahoma WSR-88D (KVNX) velocity observations (Fig. 5b). The observations used in the calculation of the azimuthal shear in the El Reno storm during the first two tornadoes were collected with beam center heights between 800 m and 3 km, so the product was restricted to the layer containing the LLM and not the tornado itself.

Overall, the low-level rotation track (Fig. 5b) also exhibited good correspondence with, and appears to support a number of features of, the vorticity swath (Fig. 5a). First, the rotation track, like the vorticity swath, was displaced slightly north of the surface damage track of Tornado B2, indicating that Tornado B2 did indeed tilt toward the north with height. Second, the rotation track indicates the presence of a strong LLM southwest of Tornado B1's surface damage track, prior to tornadogenesis (2031 UTC). We therefore consider the simulation's portrayal of this pretornadic circulation (swath V1; Fig. 5a) to be accurate. Third, the rotation track is more-or-less continuous over the gap between the surface damage tracks of Tornadoes B1 and B2, although the model's portrayal of a highly probable LLM intensification over the gap (swath V3) is only weakly supported.

b. Comparison with Oklahoma Mesonet observations

Tornado B2 passed very close to the El Reno, Oklahoma mesonet (Brock et al. 1995) station (Fig. 3a, b) and damaged part of the site (K. Ortega 2014, personal communication; also see http://ticker.mesonet.org/select.php?mo=05&da=27&yr=2011). This station, however, continued to record relative humidity (RH), aspirated air temperature, wind speed, wind direction, and atmospheric pressure every 1 min (Fig. 6). As the tornado passed, the atmospheric pressure decreased by 17 hPa at 2121 UTC (Fig. 6c), while the 1-min average wind speed at 10 m AGL increased from 10 m s^{-1} to 51 m s^{-1} (Fig. 6d). The wind direction changed from easterly to southerly until 2120 UTC as the inflow sector approached the station, before abruptly switching to northerly when the tornado passed (Fig. 6e). The station recorded a maximum wind gust of 67 m s^{-1} (not shown). If it could be shown that this gust was sustained for 3 s, this observation would correspond to EF-3 tornadic winds (McDonald and Mehta 2006).

We derived simulated observations for comparison by interpolating the model variables from the grid points closest to the El Reno mesonet station (red traces; Fig. 6a – e). We adjusted the simulated ensemble of pressure traces from the lowest model scalar level (125 m AGL) to the surface using the hydrostatic equation and the surface pressure in the initial sounding (947 hPa). This adjustment added about 13.5 hPa to the ensemble of pressure traces (Fig. 6c).

Overall, we found reasonable agreement (given the model's limitations) between the El Reno mesonet observations and simulated observations. The simulated El Reno storm cold pool is close to the observed temperature, but much drier (Fig. 6a, b). The surface temperature traces both decrease from 26 °C to about 22 or 23 °C as the mesocyclone passes (Fig. 6a). The ensemble mean RH corresponds well to the observations initially, with both tracking around 75% until 2105 UTC (Fig. 6b). During the storm passage, the mesonet RH increased to 96%, while the model ensemble mean RH decreased to less than 50%. It is believed that the low humidity in the modeled cold pools resulted from downward advection of dry midlevel air (Fig. 6c) (e.g., Dawson et al. 2010).

The passage of the El Reno tornado and mesocyclone, which appears as a sharp decrease (increase) in the observed pressure (wind speed) and an abrupt change in the wind direction around 2120 UTC, are represented in the simulations as more gradual changes in these quantities, with the extrema muted (Fig. 6c, d). The relatively coarse model grid spacing (1 km) smoothed the sharp pressure gradients responsible for the observed rapid changes.

4. ANALYSIS OF THE MERGER

The El Reno storm was unambiguously identified as a single reflectivity object at 125 m AGL (e.g., Fig. 7a, b) from 2005 to 2130 UTC. Throughout the following discussion, "the El Reno storm" refers to this reflectivity object, which is used to constrain most of the analysis products. The merging storm was identified from 2048 – 2054 UTC. For our purposes, the "merger process" starts when these two reflectivity objects first unite (2055 UTC; Fig. 7b) and ends when their associated updraft objects unite (2105 UTC; after Fig. 7e).

The vortex object corresponding to the El Reno storm's LLM was tracked as a single object from 2030 to 2117 UTC (not shown), with a brief discontinuity in the track at 2101 UTC (not shown). The MLM track also exhibited a discontinuity at 2106 UTC and jumped south at 2120 UTC. In these instances, we manually combined separate tracks into a single track. Occasionally during the procedure some of the updraft tracks were manually combined owing to the pulsing nature of supercell updrafts, their varying morphology, and simultaneity.

a. The premerger stage (2030 to 2055 UTC)

After being displaced a few km west of the LLM and near-surface vortex (hereafter NSV) at 2020 UTC (Fig. 8a), the vortex became vertically stacked by 2030 UTC (Fig. 8b), when Tornado B1 began. The NSV stayed close to the surveyed track for Tornado B1 at it progressed toward the northeast (Fig. 8b, c, d). At 2040 UTC, midway through Tornado B1's life cycle, the vortex began to tilt toward the north with height (Fig. 8c). An RFD surge at 2043 UTC (not shown) wrapped entirely around the south side of the NSV and LLM, pushing the NSV and LLM toward the east with respect to the MLM, and the MLM began to stretch and elongate toward the northwest (Fig. 8d). The El Reno storm's updraft weakened at all levels around 2046 UTC (Fig. 9a) as the ensemble mean NSV began to reintensify, producing swath V3.

In the ensemble mean, only weak (~ 5 m s^{-1}) midlevel updrafts were associated with the merging storm until 2047 UTC, when its northern outflow boundary collided with the rear flank gust front of the El Reno storm. An updraft pulse of 24 m s^{-1} occurred on the northwest side of the merging storm's reflectivity core, centered at 5 km AGL (not shown). This updraft pulse was associated with generation of enhanced near-surface ς (≥ 0.01 s^{-1}) along the colliding boundaries owing to horizontal convergence and stretching, but this area of enhanced vorticity (near x = 110 km, y = 100 km in Fig. 8e) did not merge into the NSV. The midlevel updraft (MLU) of the merging storm weakened as it approached the El Reno storm, but persisted through the merger.

The NSV intensified (ς increased from 0.02 s^{-1} to 0.03 s^{-1}) from 2047 UTC to 2050 UTC. This intensification is interpreted as the model representation of the genesis of Tornado B2, although it occurs about 4 min early relative to the NWS start time (2050 UTC). Concurrently, the MLM weakened and began to split, with its strongest lobe displaced west of the LLM (Fig. 8e). This evolution is suggestive of occluding, cyclic midlevel mesocyclogenesis followed by cyclic, low-level mesocyclogenesis.

b. The merger stage (2055 – 2105 UTC)

Starting at 2055 UTC, the merging storm and the El Reno storm were considered a single reflectivity object by the enhanced watershed algorithm (Fig. 7b). By 2100 UTC, the MLM had split into two lobes (Fig. 8f). The western lobe decoupled from and moved west of the LLM and NSV, while the eastern lobe remained stacked vertically on top of them. Near the surface, the El Reno storm's cold pool completely occluded the vortex, limiting its access to buoyant inflow (not shown).

The merger process saw an overall weakening of the El Reno storm's MLU during its interaction with several nearby MLUs. In the following discussion, we refer to four separate MLUs (numbered 1 – 4; Fig. 7c, d), which were identified by the enhanced watershed algorithm. The primary MLU of the El Reno storm (merging storm) at 2055 UTC is MLU1 (MLU2). MLU3 developed about 8 km east of MLU1 at about 2053 UTC (shown a few minutes later in Fig. 10c), and moved westward along the forward flank gust front toward MLU1 (Fig. 10a – d).

At 2056 UTC, a distinct, new updraft pulse (MLU4) developed between MLUs 1 and 2, which were separated by approximately 12 km. This "bridging" updraft formation between storm updrafts separated by more than 10 km is consistent with one category of simulated supercell-nonsupercell merger outcomes described in a forthcoming study (R. Hastings, 2014, personal communication). Straddling MLU4 was a pair of shallow, counter-rotating midlevel vortices, with the cyclonic (anticyclonic) vortex on the right (left) side of MLU4 with respect to storm motion. We presume that this vortex pair originated from MLU4's upward bending of a preexisting, crosswise, horizontal vortex line (Davies-Jones 1984). The two vortices then revolved cyclonically around MLU4, with MLU4 eventually merging into the east side of MLU3, and its cyclonic vortex eventually merging into the eastern lobe of the El Reno storm's MLM at 2100 UTC (Fig. 10b – d, Fig. 8f). MLU3 merged into MLU1 at 2059 UTC (Fig. 10d). The overall result was that the El Reno storm's MLM grew and elongated toward the northeast at 2100 UTC (Fig. 10f), having absorbed both the additional updraft area of MLU3 and the cyclonic vortex generated by MLU4.

At 2105 UTC, MLU1 and MLU2 finally joined at their easternmost contact point, restoring the comma-shaped updraft envisioned in the supercell conceptual model by Lemon and Doswell (1979), and consolidating the four separate MLUs into a single, larger MLU (shown shortly thereafter in Fig. 10f). Overall, the updraft and vortex structure of the El Reno storm remained relatively disorganized at midlevels throughout the merger process. Once the MLU merger was complete, the NSV's access to low-level buoyant air in the inflow sector was restored (not shown). Shortly thereafter, the entire mesocyclone consolidated (Fig. 10f), became vertically stacked (not shown), and intensified rapidly (Fig. 9a), with its motion becoming more easterly as it did so.

5. CONCLUSIONS

We conclude with high confidence that the storm merger (2055 to 2105 UTC) did *not* cause the handoff between Tornadoes B1 and B2 (2046 to 2050 UTC), not least because the latter preceded the former by at least five minutes. Instead, the handoff was associated with a split and rearward motion of part of the MLM, in accordance with conceptual models of occluding midlevel mesocyclone cycling put forth by Burgess et al. (1982), Dowell and Bluestein (2002b), Adlerman and Droegemeier (2005), and French et al. (2008), and others.

The El Reno storm merger process did not conform clearly to either of the merger models posited by Lee et al. (2006) or Wurman et al. (2007) (Fig. 1); additional mechanisms were also at work. In particular, the collisions between the outflow boundaries from the two storms generated additional updraft pulses. At least four separate updrafts consolidated into a single updraft over the course of approximately 10 min. In addition, a bridging midlevel updraft generated a new, small MLM that eventually merged with and augmented the MLM already present in the El Reno storm (Fig. 10a-d). The high confidence that we have in these insights was made possible by the 1-min analyses generated from the rapid PAR observations.

We speculate that the El Reno storm merger event may not be representative of mergers between a tornadic and nontornadic storm, because the details uncovered here are suggestive of a complex series of interactions between several dynamical features. We suspect that different storm mergers will proceed differently from one another, and that similar studies of additional storm merger events will need to be analyzed before a generalized conceptual model (or models) of such interactions can be synthesized.

6. ACKNOWLEDGMENTS

This work was supported by a National Research Council Research Associateship awarded to the first author. This abstract was prepared by the first author with funding provided by NOAA / Office of Oceanic and Atmospheric Research under NOAA-University of Oklahoma Cooperative Agreement #NA11OAR4320072, U.S. Department of Commerce. The statements, findings, conclusions, and recommendations are those of the author(s) and do not necessarily reflect the views of NOAA or the U.S. Department of Commerce. Vincent "Bim" Wood reviewed this manuscript internally. Manual dealiasing and quality control of the NWRT PAR data were performed by Brandon Smith and Lamont Bain (students of Kevin Manross), and Dr. Michael French. We are particularly indebted to Dr. Valliappa Lakshmanan for his assistance implementing the enhanced watershed and NEW tracking algorithms. Oklahoma Mesonet data with 1-min time resolution were provided by Dr. Kevin Kloesel, Dr. Chris Fiebrich, and Cindy Luttrell. Dr. Daniel T. Dawson II contributed the code to plot the ensemble vortex swath.

7. REFERENCES

Adlerman, E. J., and K. K. Droegemeier, 2005: The dependence of numerically simulated cyclic mesocyclogenesis upon environmental vertical wind shear. *Mon. Wea. Rev.*, **133,** 3595-3623.

Bluestein, H. B., and M. L. Weisman, 2000: The interaction of numerically simulated supercells initiated along lines. *Mon. Wea. Rev.*, **128,** 3128-3149.

Brock, F. V., K. C. Crawford, R. L. Elliott, G. W. Cuperus, S. J. Stadler, H. L. Johnson, and M. D. Eilts, 1995: The Oklahoma Mesonet: A technical overview. *J. Atmos. Oceanic Technol.*, **12,** 5-19.

Burgess, D. B., V. T. Wood, and R. A. Brown, 1982: Mesocyclone evolution statistics. *12th Conf. on Severe Local Storms*, San Antonio, Texas, American Meteorological Society, 422–424.

Coniglio, M. C., D. J. Stensrud, and L. J. Wicker, 2006: Effects of upper-level shear on the structure and maintenance of strong quasi-linear mesoscale convective systems. *J. Atmos. Sci.*, **63,** 1231-1252.

Cressman, G. P., 1959: An operational objective analysis system. *Mon. Wea. Rev.*, **87,** 367–374.

Davies-Jones, R., 1984: Streamwise vorticity: The origin of updraft rotation in supercell storms. *J. Atmos. Sci.*, **41,** 2991-3006.

Dawson, D. T., M. Xue, J. A. Milbrandt, and M. K. Yau, 2010: Comparison of evaporation and cold pool development between single-moment and multimoment bulk microphysics schemes in idealized simulations of tornadic thunderstorms. *Mon. Wea. Rev.*, **138,** 1152-1171.

Dawson, D. T., L. J. Wicker, E. R. Mansell, and R. L. Tanamachi, 2012: Impact of the environmental low-level wind profile on ensemble forecasts of the 4 May 2007 Greensburg, KS tornadic storm and associated mesocyclones. *Mon. Wea. Rev.*, **140,** 696-716.

Dowell, D. C., and H. B. Bluestein, 2002a: The 8 June 1995 McLean, Texas, storm. Part I: Observations of cyclic tornadogenesis. *Mon. Wea. Rev.*, **130,** 2626-2648.

——, 2002b: The 8 June 1995 McLean, Texas, storm. Part II: Cyclic tornado formation, maintenance, and dissipation. *Mon. Wea. Rev.*, **130,** 2649-2670.

Dowell, D. C., L. J. Wicker, and C. Snyder, 2011: Ensemble Kalman filter assimilation of radar observations of the 8 May 2003 Oklahoma City supercell: Influences of reflectivity observations on storm-scale analyses. *Mon. Wea. Rev.*, **139,** 272–294.

French, M. M., H. B. Bluestein, I. PopStefanija, C. A. Baldi, and R. T. Bluth, 2013: Reexamining the vertical development of tornadic vortex signatures in supercells. *Mon. Wea. Rev.*, **141,** 4576-4601.

French, M. M., H. B. Bluestein, D. C. Dowell, L. J. Wicker, M. R. Kramar, and A. L. Pazmany, 2008: High-resolution, mobile Doppler radar observations of cyclic mesocyclogenesis in a supercell. *Mon. Wea. Rev.*, **136,** 4997-5016.

Gaspari, G., and S. E. Cohn, 1999: Construction of correlation functions in two and three dimensions. *Quart. J. Roy. Meteor. Soc.*, **125,** 723-757.

Gilmore, M. S., J. M. Straka, and E. N. Rasmussen, 2004: Precipitation and evolution sensitivity in simulated deep convective storms: Comparisons between liquid-only and simple ice and liquid phase microphysics. *Mon. Wea. Rev.*, **132,** 1897-1916.

Hastings, R. M., and Y. P. Richardson, 2010: Storm mergers. Part 1: Preliminary numerical investigations of merger events. *25th Conf. on Severe Local Storms*, Denver, CO, American Meteorological Society, 7A.5.

Hastings, R. M., Y. P. Richardson, P. M. Markowski, and J. Wurman, 2010: Storm mergers. Part 2: Observations of merger events from VORTEX2. *25th Conf. on Severe Local Storms*, Denver, Colorado, American Meteorological Society, P8.16.

Hastings, R. M., Y. P. Richardson, P. Markowski, J. Wurman, and C. C. Weiss, 2012: Mergers in supercell environments. Part I: Conceptual models of mechanisms governing merger outcomes. *26th Conf. on Severe Local Storms*, Nashville, Tennessee, American Meteorological Society, 11B.16.

Heinselman, P. L., and S. M. Torres, 2011: High-temporal-resolution capabilities of the National Weather Radar Testbed phased-array radar. *J. Climate Appl. Meteor.*, **50,** 579-593.

Heinselman, P. L., D. L. Priegnitz, K. L. Manross, T. M. Smith, and R. W. Adams, 2008: Rapid sampling of severe storms by the National Weather Radar Testbed Phased Array Radar. *Wea. Forecasting*, **23,** 808-824.

Hunt, B. R., E. J. Kostelich, and I. Szunyogh, 2007: Efficient data assimilation for spatiotemporal chaos: A local ensemble transform Kalman filter. *Physica D: Nonlinear Phenomena*, **230,** 112-126.

Illingworth, A. J., J. W. F. Goddard, and S. M. Cherry, 1987: Polarization radar studies of precipitation development in convective storms. *Quart. J. Roy. Meteor. Soc.*, **113,** 469-489.

Jewett, B. F., B. D. Lee, and R. B. Wilhelmson, 2002: Numerical simulation of cell interaction. *21st Conf. on Severe Local Storms*, San Antonio, TX, American Meteorological Society, 353-356.

Klemp, J. B., P. S. Ray, and R. B. Wilhelmson, 1980: Analysis of merging storms on 20 May 1977. *19th Conf. on Radar Meteorology*, Miami Beach, Florida, American Meteorological Society, 317 - 324.

Kogan, Y. L., and A. Shapiro, 1996: The simulation of a convective cloud in a 3D model with explicit microphysics. Part II: Dynamical and microphysical aspects of cloud merger. *J. Atmos. Sci.*, **53,** 2525-2545.

Kumjian, M. R., and A. V. Ryzhkov, 2008: Polarimetric signatures in supercell thunderstorms. *J. Climate Appl. Meteor.*, **47,** 1940-1961.

Lakshmanan, V., and T. Smith, 2010: An objective method of evaluating and devising storm-tracking algorithms. *Wea. Forecasting*, **25,** 701-709.

Lakshmanan, V., K. Hondl, and R. Rabin, 2009: An efficient, general-purpose technique for identifying storm cells in geospatial images. *J. Atmos. Oceanic Technol.*, **26,** 523-537.

Lee, B. D., B. F. Jewett, and R. B. Wilhelmson, 2006: The 19 April 1996 Illinois tornado outbreak. Part II: Cell mergers and associated tornado incidence. *Wea. Forecasting*, **21,** 449-464.

Lemon, L. R., and C. A. Doswell, 1979: Severe thunderstorm evolution and mesocyclone structure as related to tornadogenesis. *Mon. Wea. Rev.*, **107,** 1184-1197.

Lin, Y.-L., R. D. Farley, and H. D. Orville, 1983: Bulk parameterization of the snow field in a cloud model. *J. Appl. Meteor.*, **22,** 1065-1092.

Lindsey, D. T., and M. J. Bunkers, 2005: Observations of a severe, left-moving supercell on 4 May 2003. *Wea. Forecasting*, **20,** 15-22.

McDonald, J. R., and K. C. Mehta, 2006: *A Recommendation for an Enhanced Fujita Scale (EF-Scale)*. Texas Tech University, Lubbock, Texas, 111 pp. [Available from http://www.depts.ttu.edu/weweb/EFScale.pdf.%5D.

Miller, M. L., V. Lakshmanan, and T. M. Smith, 2012: An automated method for depicting mesocyclone paths and intensities. *Wea. Forecasting***,** in press.

Miyoshi, T., 2010: The Gaussian approach to adaptive covariance inflation and its implementation with the local ensemble transform Kalman filter. *Mon. Wea. Rev.*, **139,** 1519-1535.

National Weather Service, 2012: Information for the Tornado Outbreak of May 24, 2011. http://www.srh.noaa.gov/oun/?n=events-20110524, retrieved on 17 December 2012.

Ott, E., B. R. Hunt, I. Szunyogh, A. V. Zimin, E. J. Kostelich, M. Corazza, E. Kalnay, D. J. Patil, and J. A. Yorke, 2004: A local ensemble Kalman filter for atmospheric data assimilation. *Tellus A*, **56,** 415-428.

Oye, R., C. Mueller, and S. Smith, 1995: Software for radar translation, visualization, editing, and interpolation. *27th Conf. on Radar Meteorology*, Vail, Colorado, American Meteorological Society, 359 - 361.

Romine, G. S., D. W. Burgess, and R. B. Wilhelmson, 2008: A dual-polarization-radar-based assessment of the 8 May 2003 Oklahoma City area tornadic supercell. *Mon. Wea. Rev.*, **136,** 2849-2870.

Snyder, J. C., A. Ryzhkov, M. R. Kumjian, and J. Picca, 2014: Using the ZDR column product to detect updraft development and track updraft evolution. *27th Conf. on Severe Local Storms*, Madison, Wisconsin, American Meteorological Society, 16A.15.

Stensrud, D. J., and J. Gao, 2010: Importance of horizontally inhomogeneous environmental initial conditions to ensemble storm-scale radar data assimilation and very short-range forecasts. *Mon. Wea. Rev.*, **138,** 1250-1272.

Wakimoto, R. M., and N. T. Atkins, 1996: Observations on the origins of rotation: The Newcastle Tornado during VORTEX 94. *Mon. Wea. Rev.*, **124,** 384-407.

Wakimoto, R. M., N. T. Atkins, and J. Wurman, 2011: The LaGrange tornado during VORTEX2. Part I: Photogrammetric analysis of the tornado combined with single-Doppler radar data. *Mon. Wea. Rev.*, **139,** 2233-2258.

Westcott, N. E., and P. C. Kennedy, 1989: Cell development and merger in an Illinois thunderstorm observed by Doppler radar. *J. Atmos. Sci.*, **46,** 117-131.

Wurman, J., Y. Richardson, C. Alexander, S. Weygandt, and P. F. Zhang, 2007: Dual-Doppler and single-Doppler analysis of a tornadic storm undergoing mergers and repeated tornadogenesis. *Mon. Wea. Rev.*, **135,** 736-758.

Zrnić, D. S., J. F. Kimpel, D. E. Forsyth, A. Shapiro, G. Crain, R. Ferek, J. Heimmer, W. Benner, T. J. McNellis, and R. J. Vogt, 2007: Agile-beam phased array radar for weather observations. *Bull. Amer. Meteor. Soc.*, **88,** 1753-1766.

Table 1. Partial list of NCOMMAS parameters.

Parameter	*Value(s)*
Model initial time	1930 UTC 24 May 2011
Assimilation window	1940 – 2000 UTC 24 May 2011 (KTLX volumes) 2000 – 2130 UTC 24 May 2011 (PAR volumes)
Assimilation cycle frequency	5 min (KTLX volumes) 1 min (PAR volumes)
Observations assimilated	V_r, Z
Ensemble members	48
Simulation domain	180 km x 180 km x 22 km
Domain size	181 x 181 x 56
Southwest corner of domain	34.52 °N, 99.43 °W
Model bottom boundary	370 m MSL
Horizontal grid spacing	1 km
Vertical grid spacing	250 m at and below 4.1 km AGL; stretched above to a maximum of 700 m at 22.0 km AGL
First scalar level	125 m AGL
Cloud microphysical scheme	Lin-Farley-Orville (Lin et al. 1983; Gilmore et al. 2004)
Rain density ρ_r	1000 kg m^{-3}
Rain intercept parameter N_{0r}	8.0×10^5 m^{-4}
Hail density ρ_h	900 kg m^{-3}
Hail intercept parameter N_{0h}	4.0×10^4 m^{-4}
Snow density ρ_s	100 kg m^{-3}
Snow intercept parameter N_{0s}	3.0×10^6 m^{-4}
Lateral boundaries	Open
Model time step	1 s
Assumed observation error variance for Z (σ_z^2) and V_r (σ_{vr}^2)	$(10.0\ \text{dBZ})^2$, $(2.0\ \text{m s}^{-1})^2$
Covariance localization radius (Gaspari and Cohn 1999)	Horizontal: 3000 m Vertical: 1500 m

Table 2. Object identification algorithm parameters used on the ensemble mean fields.

Object	Variable	Height (AGL)	Minimum	Maximum	Saliency
Storm	*Z*	125 m	35 dBZ	70 dBZ	80 km^2
Low-level mesocyclone	ς (u, v)	1 km	4.0×10^{-3} s^{-1}	18.0×10^{-3} s^{-1}	1 km^2
Updraft	*w*	5 km	10 m s^{-1}	60 m s^{-1}	2 km^2

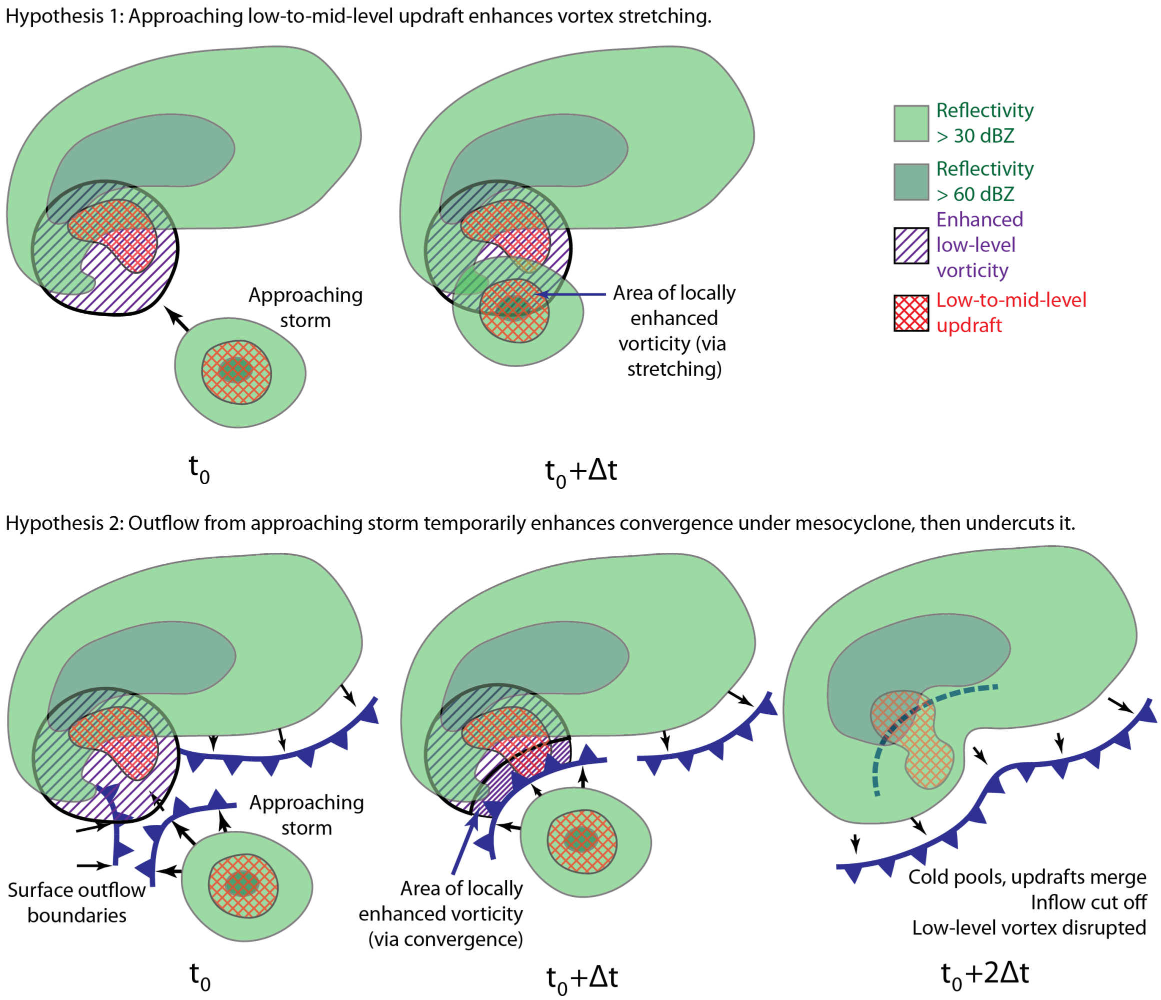

Fig. 1. Two hypotheses for how storm interactions may change low-level vorticity in a supercell, based upon suggestions offered by (a) Lee et al. (2006) and (b) Wurman et al. (2007). Reflectivity values are approximations used to orient the reader to the storm structure.

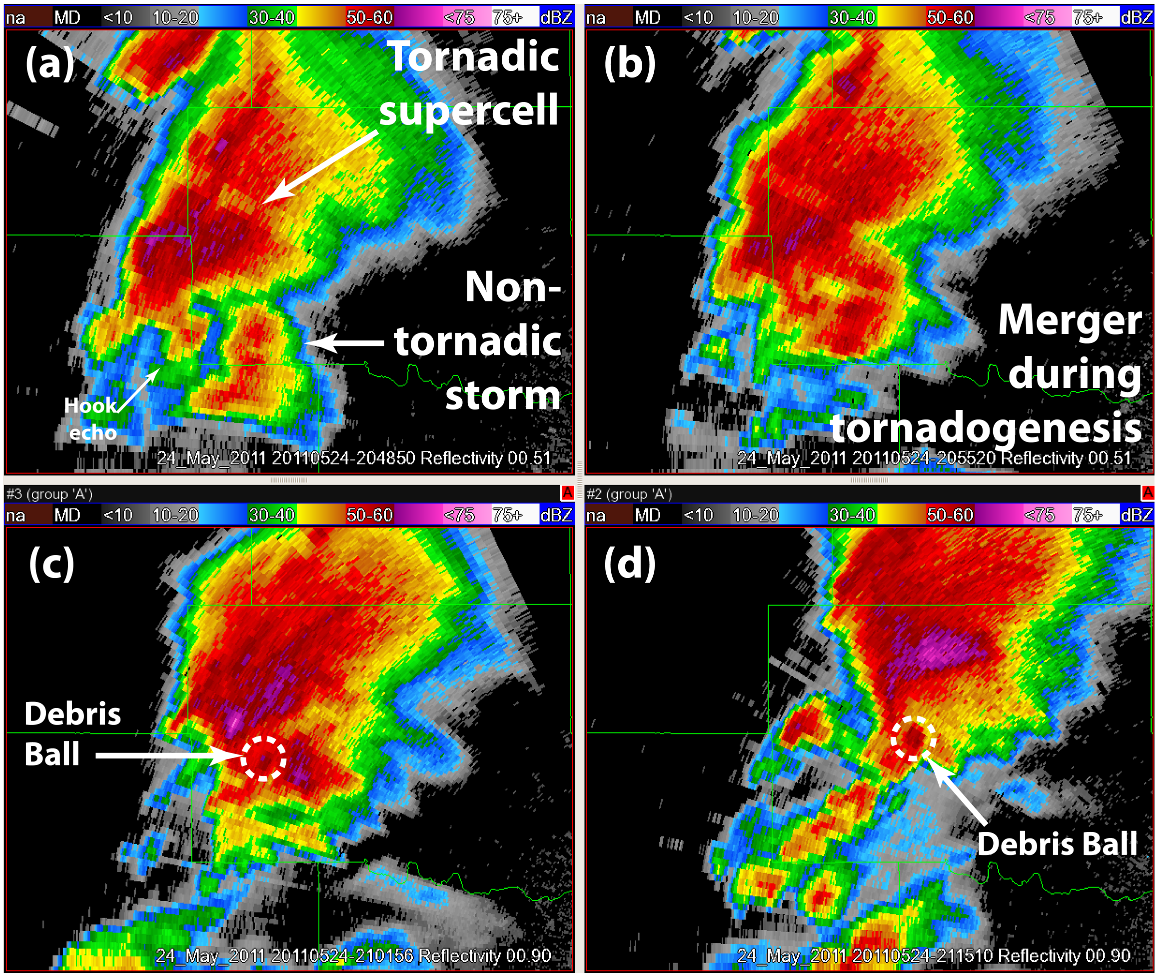

Fig. 2. Merger between a tornadic supercell and a nontornadic storm west of El Reno, Oklahoma on 24 May 2011 as observed by the PAR at (a) 2049 UTC, (b) 2055 UTC, (c) 2102 UTC and (d) 02115 UTC. An EF-3 tornado ended at 2046 UTC, just prior to panel (a), while an EF-5 tornado began 2050 UTC, between panels (a) and (b). The "debris ball" of the developing EF-5 tornado, which is about 70 km from the PAR, is denoted by a dashed white circle in panels (c) and (d). Reflectivity is in dBZ; the radar elevation angle is 0.5°.

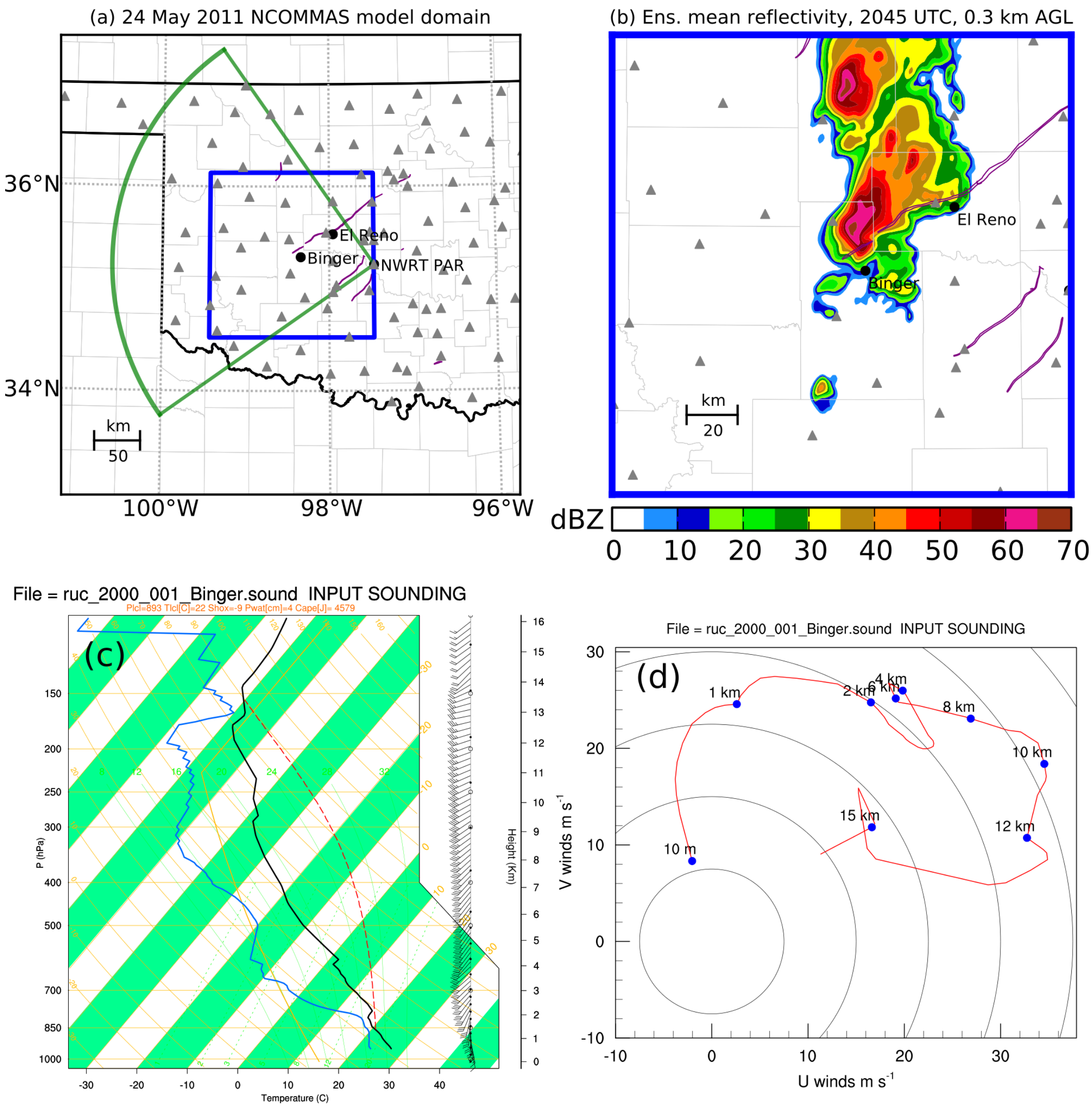

Fig. 3. (a) Map of western and central Oklahoma (outlined in black) showing the NCOMMAS model domain for this study (blue box), the NWRT PAR coverage area (sector outlined in green), tornado tracks (purple outlines, courtesy of the NWS WFO in Norman, Oklahoma), and Oklahoma mesonet stations (gray triangles). The track of tornado B1 is north of Binger, while the track of Tornado B2 passes by El Reno. Other tornadoes whose tracks are depicted are not the focus of this study. (b) Ensemble mean reflectivity (filled color contours in dBZ) in the domain shown in (a) at 2045 UTC at 375 m AGL. County boundaries in both panels (a) and (b) are drawn in thin gray lines. (c) Skew-T log-p diagram of the sounding used to generate the ensemble of initial model states. (d) Hodograph for the wind profile shown in (c).

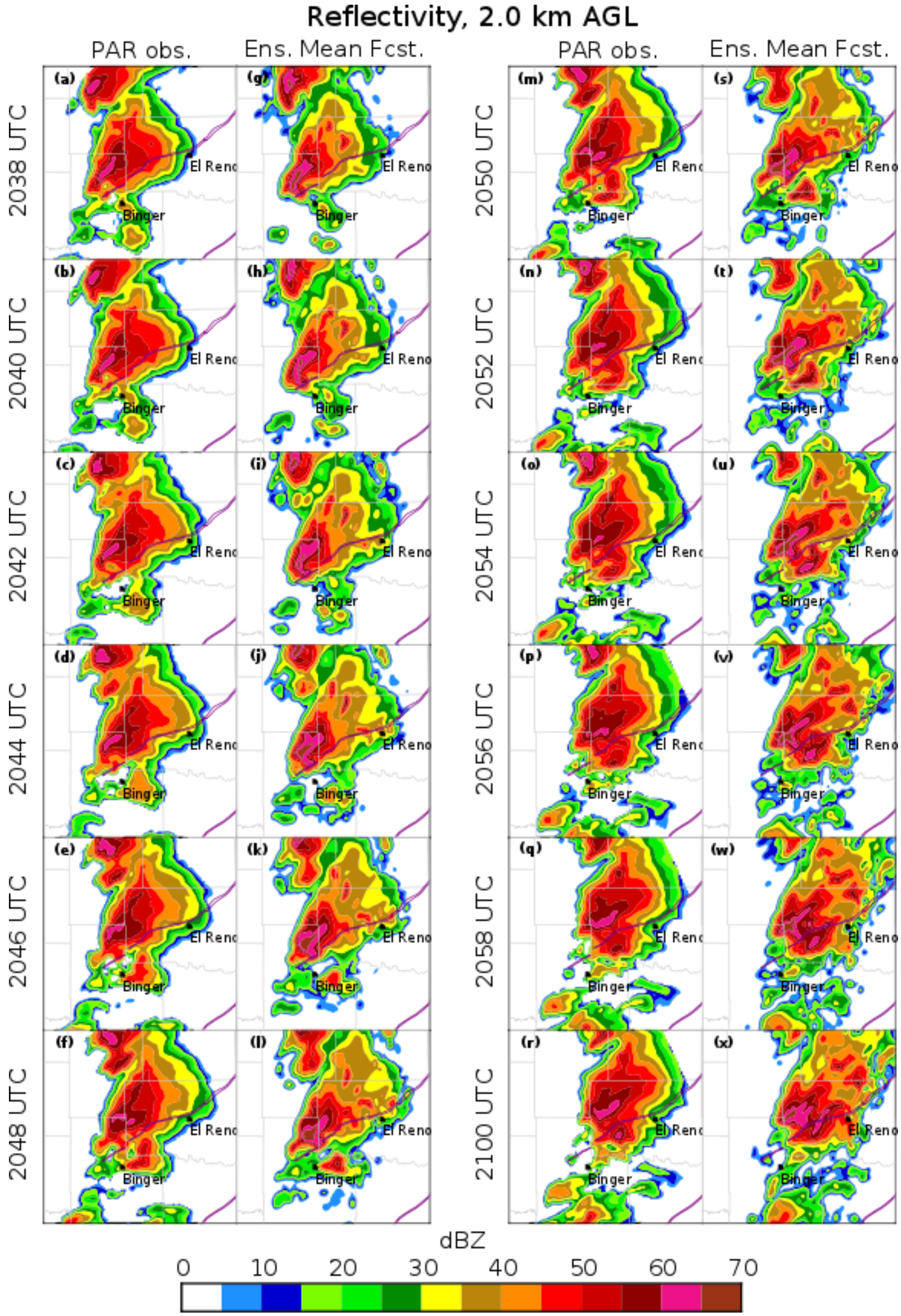

Fig. 4. (a – f and m – r) Observed NWRT PAR reflectivity (objectively analyzed to a 1 km grid) and (g – l and s – x) ensemble mean forecast reflectivity (in dBZ) in the El Reno storm at 2.0 km AGL plotted at 2-min intervals from 2038 to 2100 UTC. The cell merger under investigation occurs northeast of Binger around 2050 UTC. Each panel shows a subdomain, 100 km on a side, of the domain depicted in Fig. 3(a).

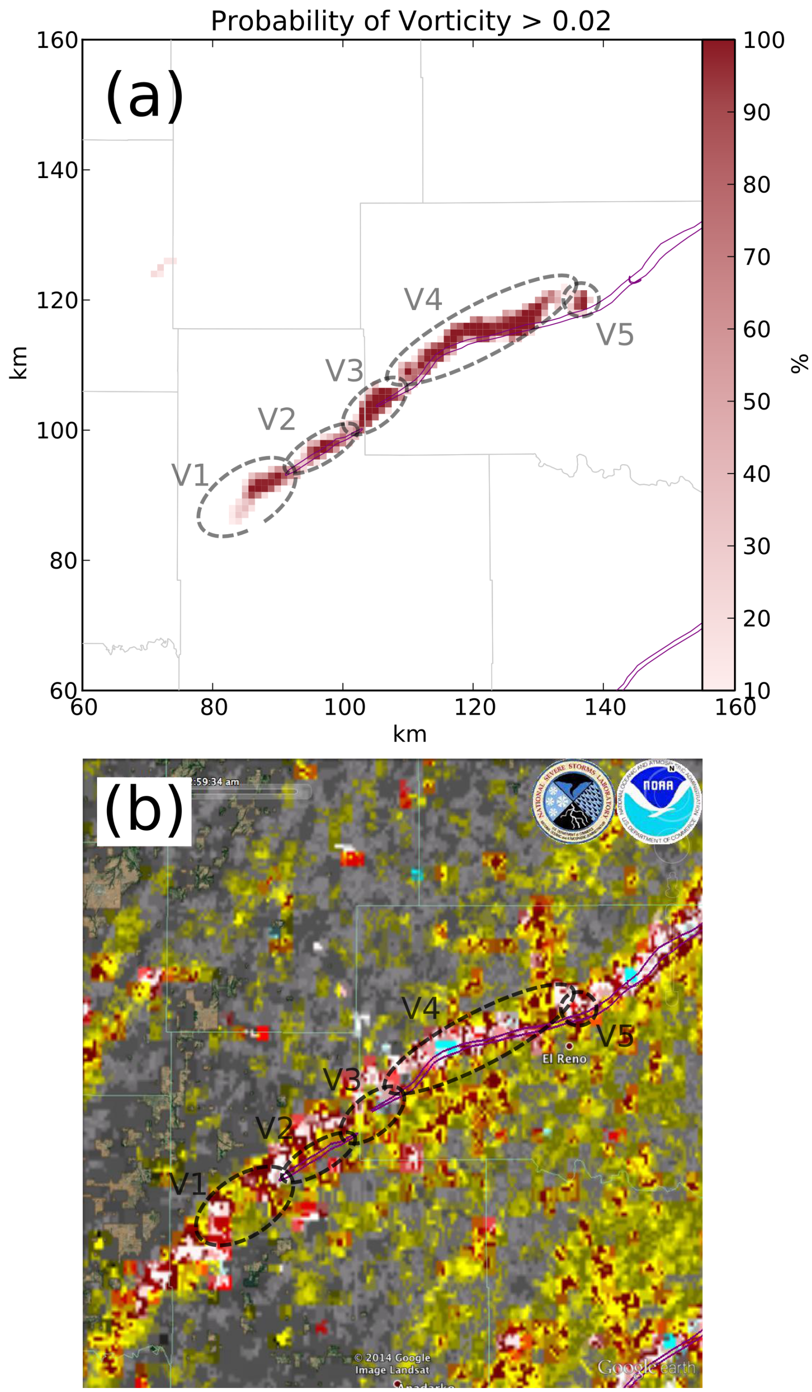

Fig. 5. (a) Probabilistic vorticity swath generated from the 48-member ensemble at 1 km AGL. Red shading denotes the probability that the vorticity at that grid point exceeded 0.02 s^{-1} some time between 2030 and 2130 UTC. The swath is broken up into several segments, labeled V1 through V5. Tornado tracks and county outlines are plotted as in Fig. 3(b). The plot shows a subdomain, 100 km on a side, of the domain displayed in Fig. 3(b). Low-level rotation track product generated from KTLX observations of the El Reno storm, consisting of accumulated maximum azimuthal shear observed in the 0-to-3 km AGL layer (Miller et al. 2012). This product can be obtained from https://www.nssl.noaa.gov/about/history/2011/. Swath segments from panel (a) are overlaid on panel (b) for comparison. Tornado tracks are outlined in purple; counties are outlined in cyan. Distances shown are in km relative to the southwest corner of the model domain (Fig. 3b).

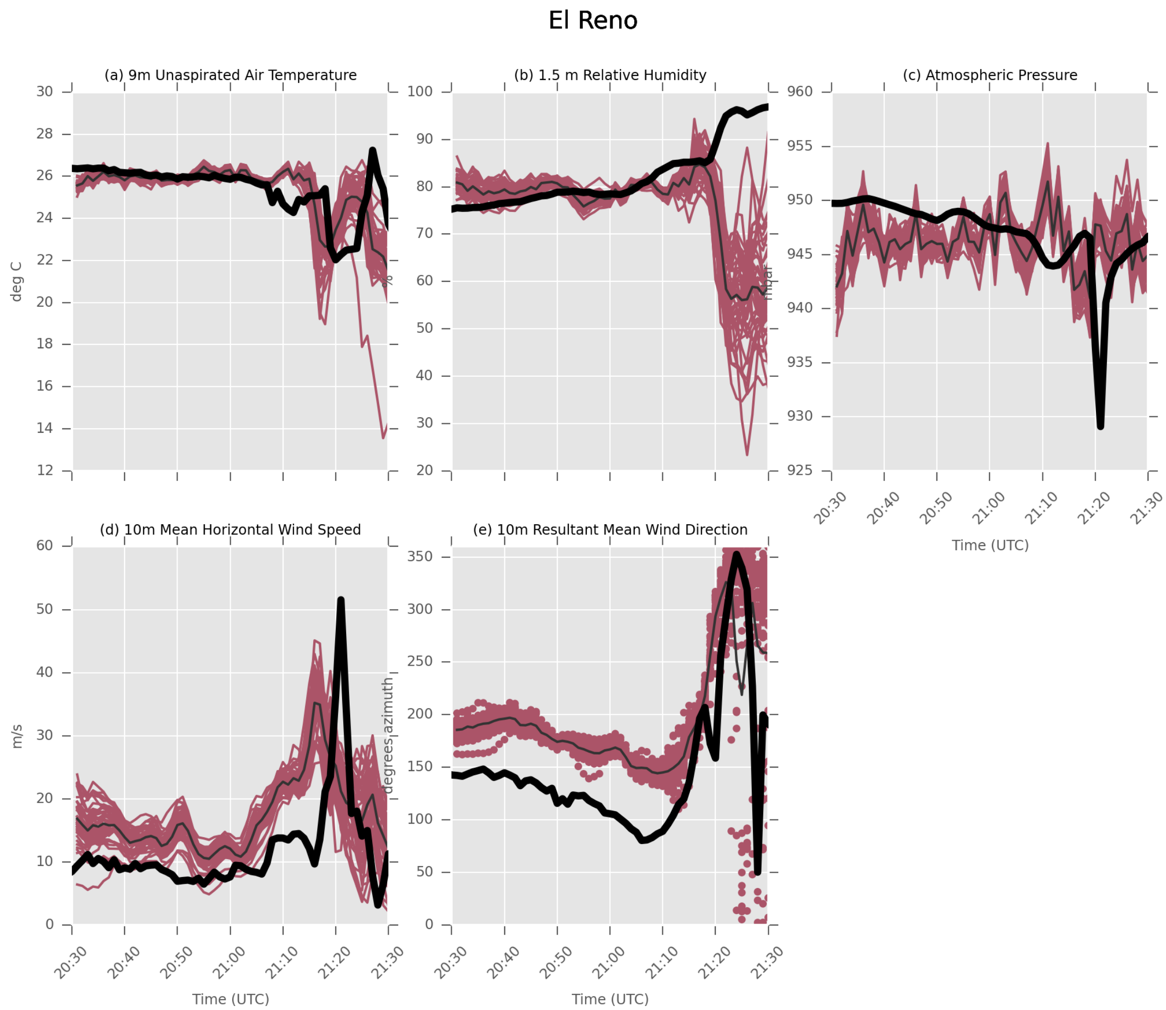

Fig. 6. El Reno, Oklahoma Mesonet measurements (thick black lines) of (a) air temperature (°C) at 9 m AGL, (b) RH (in percent) at 1.5 m AGL, (c) atmospheric pressure (hPa), and (d) horizontal wind speed (m s^{-1}) and (e) direction (°) at 10 m AGL, overlaid on top of the ensemble of simulated variables (red lines) taken at the model grid point closest to the El Reno mesonet station at the lowest scalar level (125 m AGL). Because of the 360° wraparound, ensemble wind directions are plotted as points instead of lines. The thin black line in the middle of each bundle of red lines (or points) is the ensemble mean.

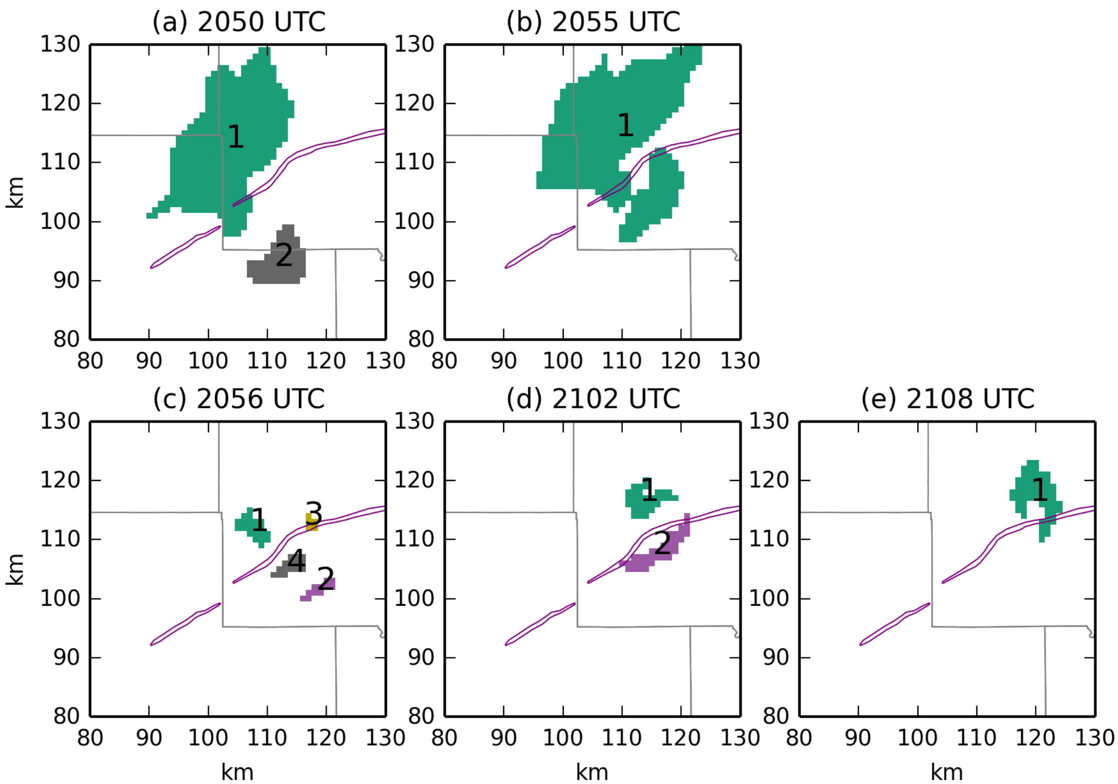

Fig. 7. (a, b) Reflectivity objects at 125 m AGL for (1) the El Reno storm and (2) the merging storm (a) before the merger, and (b) at the beginning of the merger phase. (c, d, e) Updraft objects at 5 km AGL at (c) the beginning of the merger, (d) partway through the merger, and (e) after the merger. Objects not associated with the merger process are not plotted. Tornado tracks are outlined in purple. County outlines are drawn in thin gray lines. Distances shown on the axes are in km relative to the southwest corner of the model domain (Fig. 3b).

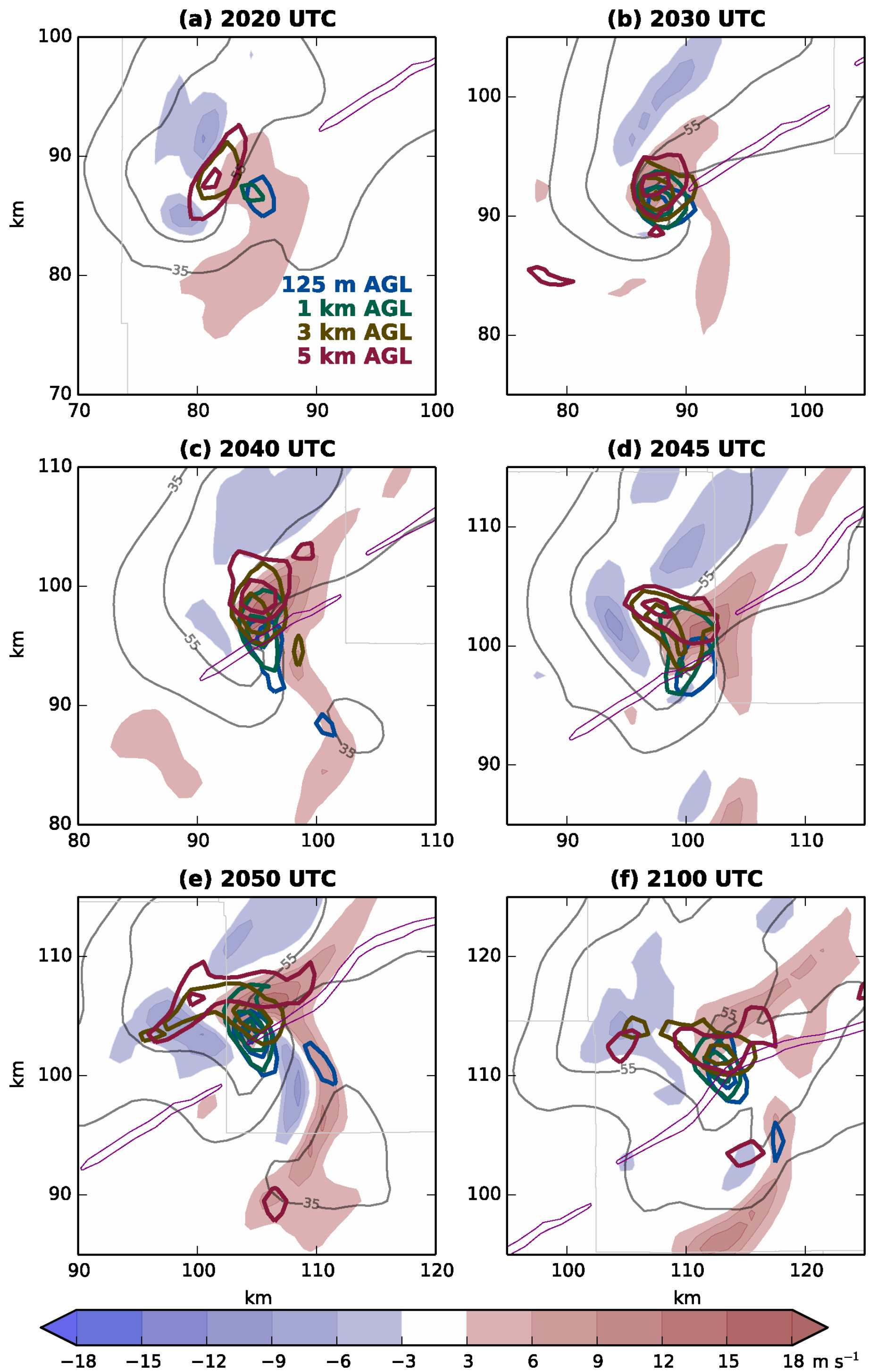

Fig. 8. Ensemble mean surface reflectivity (gray contours at 35 and 55 dBZ), vertical velocity at 625 m AGL (filled color contours in intervals of 3 m s^{-1}), and vertical vorticity (contours in intervals of 0.01 s^{-1} starting from +0.01 s^{-1}) near the surface (blue, the NSV), at 1 km AGL (green, the LLM), at 3 km AGL (yellow, an intermediate level between the LLM and MLM), and at 5 km AGL (red, the MLM) plotted at (a) 2020 UTC, (b) 2030 UTC, (c) 2040 UTC, (d) 2045 UTC, (e) 2050 UTC) and (f) 2100 UTC. For clarity, only positive vorticity contours are plotted. Tornado tracks are outlined in purple. County outlines are drawn in thin gray lines. Distances shown on the axes are in km relative to the southwest corner of the model domain (Fig. 3b).

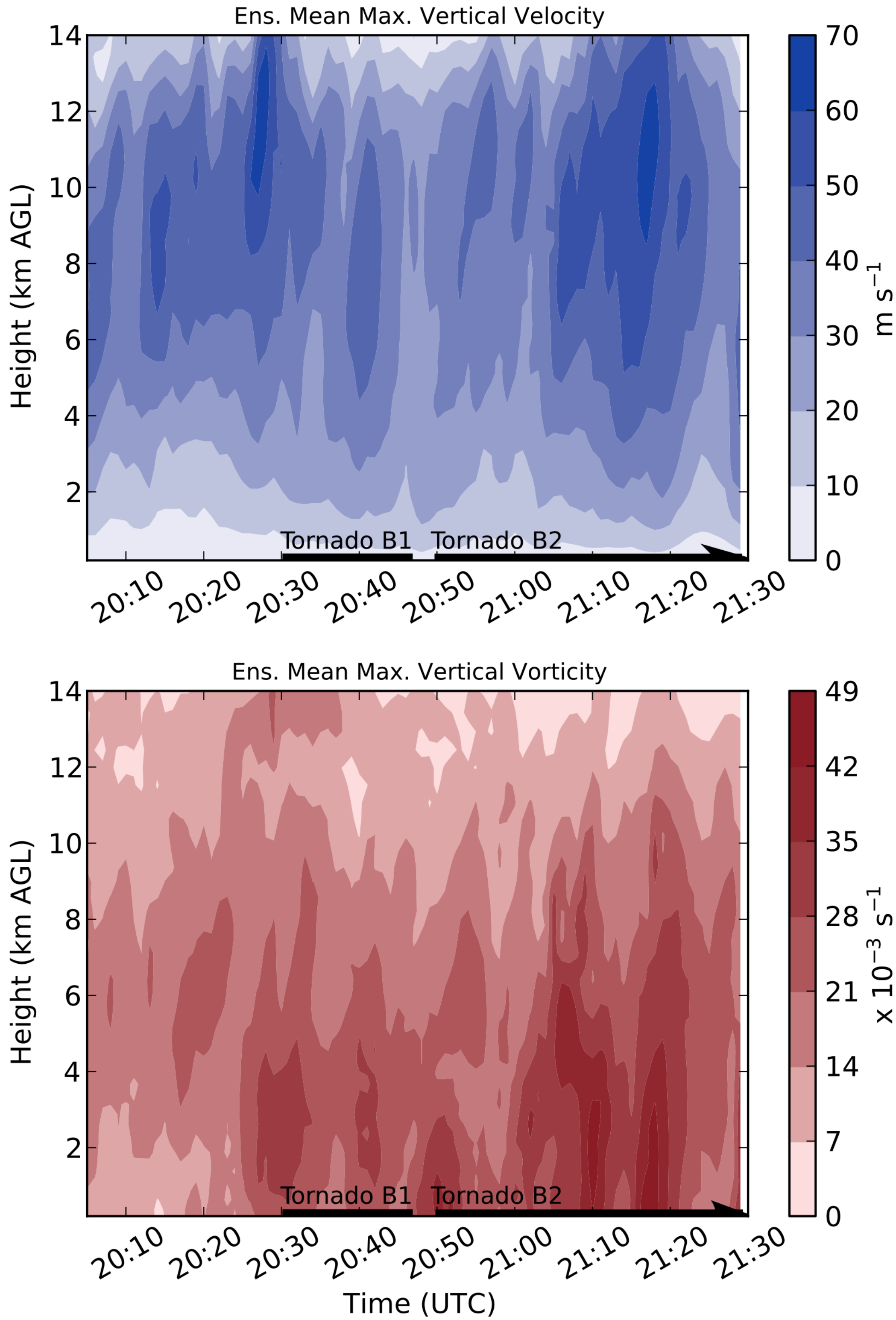

Fig. 9. Time-height plots of (a) ensemble mean maximum vertical velocity (filled blue contours) and (b) ensemble mean maximum vertical vorticity (filled red contours) in the El Reno storm (reflectivity object dilated by 3 grid points to ensure inclusion of the bounded weak echo region). The times of tornadoes B1 and B2 are annotated on the bottom axes as solid black lines.

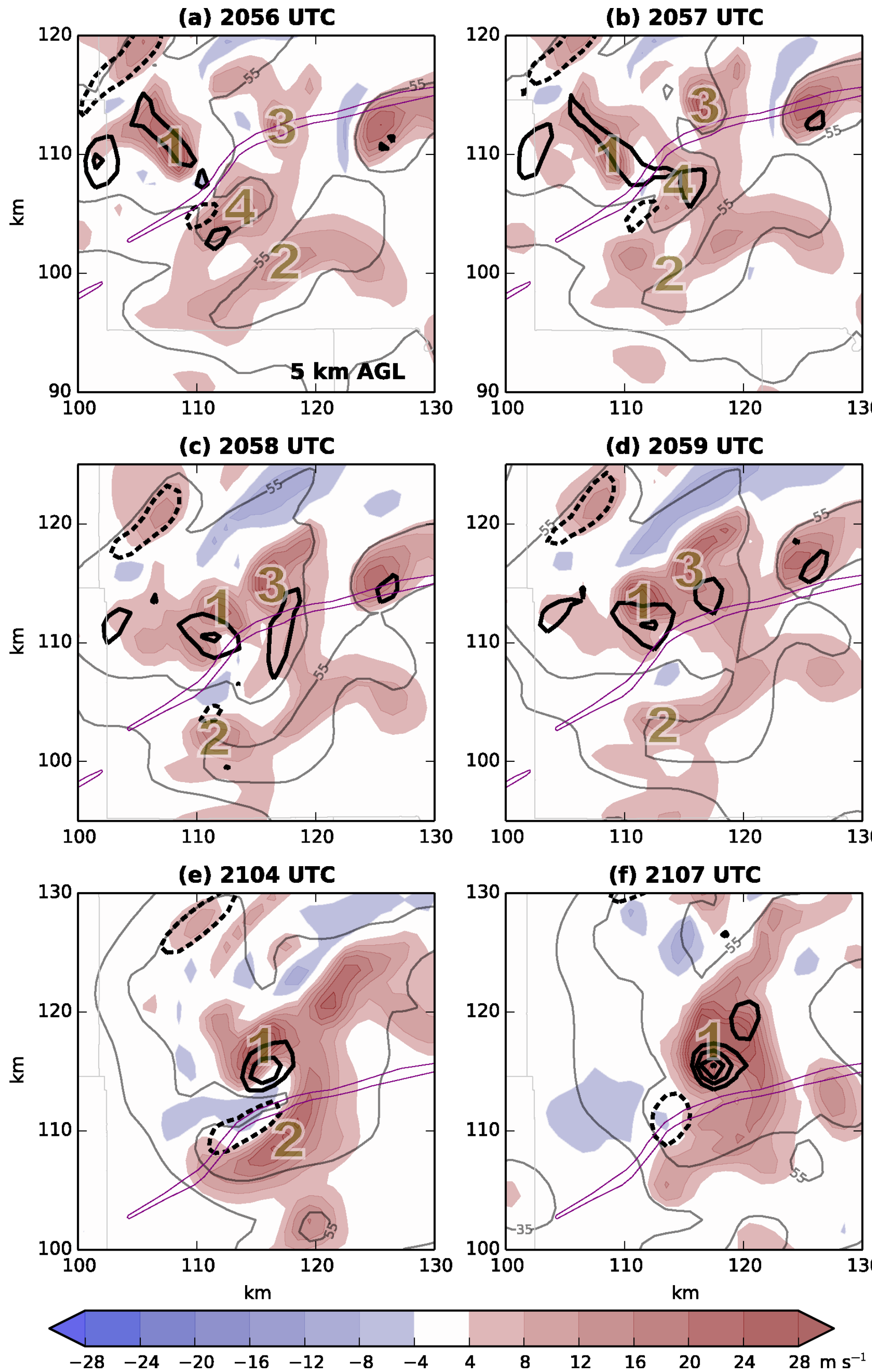

Fig. 10. Ensemble mean reflectivity (gray contours at 35 and 55 dBZ), vertical velocity (filled color contours in intervals of 4 m s^{-1}), and vertical vorticity (thick black contours in intervals of 0.01 s^{-1}, with the zero contour suppressed for clarity and dashed contours representing negative values) at 5 km AGL plotted at (a) 2056 UTC, (b) 2057 UTC, (c) 2058 UTC, (d) 2059 UTC, (e) 2104 UTC, and (f) 2107 UTC. Four updrafts (Fig. 7c) have been numbered for reference. Tornado tracks are outlined in purple. County outlines are drawn in thin gray lines. Distances shown on the axes are in km relative to the southwest corner of the model domain (Fig. 3b).